Structures 34 (2021) 4803–4813

Contents lists available at ScienceDirect

Structures

journal homepage: www.elsevier.com/locate/structures

Nonlinear bending analysis of fgp plates under various boundary conditions using an analytical approach

Pham Thanh Tung [a], Nguyen Van Long [a,*], Tran Minh Tu [a], Nguyen Thi Bich Phuong [a], Le Thanh Hai [b], Tran Ngoc Long [b]

[a] National University of Civil Engineering, 55 Giai Phong Road, Hanoi, Viet Nam
[b] Vinh University, 182 Le Duan Road, Vinh, Nghe An, Viet Nam

ARTICLE INFO

Keywords:
Analytical approach
First-order shear deformation theory
FGP plates
Neutral surface position concept
Nonlinear bending

ABSTRACT

In this paper, the nonlinear bending behavior of functionally graded porous (FGP) plates under uniformly distributed transverse loads is studied based on the neutral surface concept within the framework of first-order shear deformation theory (FSDT) including geometrical nonlinearity. The FGP materials with three porosity distribution patterns namely uniform, non-uniform symmetric and non-uniform asymmetric are considered. Using the stress function and Galerkin method, the analytical solutions are obtained to examine the load vs deflection and load vs bending moment curves for various edges boundary conditions. The present results are compared with reference solutions to show the accuracy and the effectiveness of the proposed approach. The effects of the geometric, material parameters, elastic foundations and in-plane constraints on the nonlinear bending behavior of FGP plates are studied in detail through numerical investigations.

1. Introduction

In modern life, the demand for finding and analyzing new materials with distinctive properties in comparison with the traditional ones has become prevalent. The functionally graded porous materials (FGPMs) are known as an important category of lightweight materials with very good energy absorption capability, low specific weight, energy dissipation reduction, heat resistance, etc [1–5]. In terms of FGMs, the porosity distributions are formed by continuously changing the internal pore size and density within the porous structures, so that a smooth change in mechanical properties is achieved. The FGP structures have wide applications in various engineering branches such as aviation, automobile, shipbuilding, defence industries and civil construction. Therefore, a deep understanding of mechanical responses relating to these structures has drawn the scholars' attention.

Magnucki et al. [6] presented an analytical solution to analyze bending and buckling behaviors of rectangular FGP plates, the obtained results are validated with the finite element (FE) model using ANSYS. Chen et al. [7] analyzed the static and buckling behavior of Timoshenko FGP beams by the Ritz method. The exact solution for natural frequencies of the FGP thick panel is presented by Rezae and Saidi in [8]. Arani et al. [9] used DQM (differential quadrature method) in conjunction with higher-order shear deformation theory (HSDT) to predict natural frequencies of the FGP rectangular plate rested on the Winkler elastic foundation. Akbas [10] explored the porosity effect on the free vibration and bending response of FG plates. Wattanasakulpong et al. [11] predicted natural frequencies of FGP beams basing on the third-order shear deformation theory (TSDT) by the Chebyshev collocation method. The analytical solutions for static analyses of FG beam with porosity rested on elastic foundation has been formulated by Phuong et al. in [12]. Demirhan and Taskin [13] investigated the bending characteristic and natural frequencies of FGP plates subjected to the Levy type of boundary condition. Zhao et al. [14] used an improved Fourier series method to analyze the free vibration of the Mindlin porous plate. Rad et al. [15] investigated the buckling response of rectangular FGP plates by an analytical approach using FSDT and Reddy's HSDT.

Besides the linear analysis of structures, nonlinear analysis is carried out by many authors because it reflects more accurately how the structure works in practice. Using a 3-D FEM, Shen [16], Na and Kim [17] analyzed the nonlinear bending behavior of FG plates under mechanical load in a thermal environment. Yu et al. [18] implemented a geometrically nonlinear analysis of FG plates using isogeometric analysis (IGA) in combination with simple FSDT. Dong and Li [19] studied

* Corresponding author.
E-mail address: longnv@nuce.edu.vn (N.V. Long).

https://doi.org/10.1016/j.istruc.2021.10.042
Received 16 May 2021; Received in revised form 29 August 2021; Accepted 12 October 2021

the effect of material heterogeneity, temperature, and geometrical dimension on static, buckling and vibration characteristics of porous plates by employing the unified nonlinear analytical solution. Using smoothed finite element technique, Kumar et al. [20] implemented linear and nonlinear analyses of Mindlin quadrilateral composite plates. Based on the sinusoidal shear deformation plate theory, the nonlinear bending behaviour of FG multilayered graphene platelet-reinforced - composite plates is investigated by Gholami and Ansari [21] by using the generalized differential quadrature (GDQ) method. Nguyen et al. [22] explored the effects of porosity patterns and porosity volume fractions on the bending and dynamic characteristics of FG plates with porosities using the polygonal FEM. Duc et al. [23] presented the nonlinear transient analysis of FGP plates subjected to thermo-mechanical loads resting on Pasternak's elastic foundation. Post-buckling response of FGP plate resting on Pasternak's foundations subjected to mechanical loads in thermal environment is studied analytically by Cong et al. [24] implementing Reddy's HSDT. Huang et al. [25] presented nonlinear dynamic vibrations of FGP plates by using a semi-analytical method and asymptotic solutions based on HSDT. Using the Galerkin method, Gao et al. [26] analyzed nonlinear dynamic buckling of porous beams. Keleshteri and Jelovica [27] analyzed large amplitude free vibration of porous cylindrical panels subjected to various boundary conditions employing different shell theories. Nonlinear free vibrations of stiffened FGP annular spherical shells rested on Pasternak's foundation are examined by Mirjavadi et al. [28]. Xie et al. [29] adopted the energy balance method to predict nonlinear frequencies of FG plates with porosities. Tu et al. [30] explored post-buckling behaviors of FGP plates including initial geometrical imperfection by using an analytical approach. Hung et al. [31] investigated the non-linear buckling and post-buckling behavior of FGP variable thickness toroidal shell segments surrounded by elastic foundation subjected to axial compressive loads using Donnell shell theory. Using variational differential quadrature finite element method, Ansari et al. [32] studied the geometrically nonlinear static bending of FG graphene platelet-reinforced composite porous plates with arbitrary shape. Liu et al. [33] presented the iso-geometric analysis based on a simple first-order shear deformation theory (S-FSDT) to investigate geometrically nonlinear free vibration, nonlinear static bending and transient dynamic response of FGP plates integrated with piezoelectric composite layers in the thermal environment. Mahesh et al. [34] predicted large/nonlinear deflection of FG magneto-electro-elastic porous flat panels using HSDT and finite element method.

From the above-mentioned review, it can be seen that studies regarding nonlinear bending of FGP plate are still very limited. Therefore, this paper's aimis to enrich this field. Based on FSDT and by introducing the physical neutral surface position concept, the governing equations in terms of displacements and Airy's stress function are obtained in a simple form, reducing the computational time, which is particularly effective for nonlinear problems. The Galerkin method and solution in Fourier series form is applied to give the nonlinear partial differential equations, which can be solved directly with a semi-analytical method. After validating the proposed model, the influence of various material parameters, geometric parameters, elastic foundation, and in-plane constraints on the nonlinear bending response of FGP plates are investigated through parametric studies.

2. The functionally graded porous plate

Consider a rectangular FGP plate of thickness h, dimensions in x, y - axes are length a, and width b, respectively as shown in Fig. 1-a. The plate is rested on the Pasternak's elastic foundation with stiffness coefficients: K_w - Winkler stiffness, K_{si} $(i = x, y)$ - shear stiffness.

In this paper, the open-cell porous materials with three porosity distribution patterns (Fig. 2) are considered, the material properties are expressed as following [35,36]:

For uniform distribution (Type 1 - Fig. 2-a):

$$\{E, G\} = \{E_1^*, G_1^*\}(1 - e_0\chi); \chi = \frac{1}{e_0} - \frac{1}{e_0}\left(\frac{2}{\pi}\sqrt{1 - e_0} - \frac{2}{\pi} + 1\right)^2 \tag{1}$$

For non-uniform symmetric distribution (Type 2 - Fig. 2-b):

$$\{E(z), G(z)\} = \{E_1^*, G_1^*\}[1 - e_0 cos(\pi z/h)] \tag{2}$$

For non-uniform asymmetric distribution (Type 3 - Fig. 2-c):

$$\{E(z), G(z)\} = \{E_1^*, G_1^*\}\left[1 - e_0 cos\frac{1}{2}(\pi z/h + \pi/2)\right] \tag{3}$$

where e_0 is the porosity coefficient and defined by:

$$e_0 = 1 - \frac{E_2^*}{E_1^*} = 1 - \frac{G_2^*}{G_1^*}; \quad (0 < e_0 < 1) \tag{4}$$

in which E_1^*, G_1^* are maximum values of Young's modulus and shear modulus and similarly, E_2^*, G_2^* are minimum values, respectively. The extremum values of Young's moduli are related to the extremum values of shear moduli by $G_i^* = E_i^*/[2(1 + \nu)]$. Assume that Poisson coefficient ν is constant along the plate thickness.

When analyzing the FG one- or two-dimensional structures, the mid-surface formulation is most commonly used. However, several studies have indicated that by using the neutral surface formulation, governing equations for structures become simpler because stretching-bending couplings are eliminated [37–39].

For the FGP plate with asymmetric distribution pattern, the neutral surface location has not coincided with the middle surface, and is indicated from the condition [37]:

$$\int_{-h/2}^{h/2}(z - C)E(z)dz = 0 \quad \Rightarrow C = \frac{\int_{-h/2}^{h/2} zE(z)dz}{\int_{-h/2}^{h/2} E(z)dz} \tag{5}$$

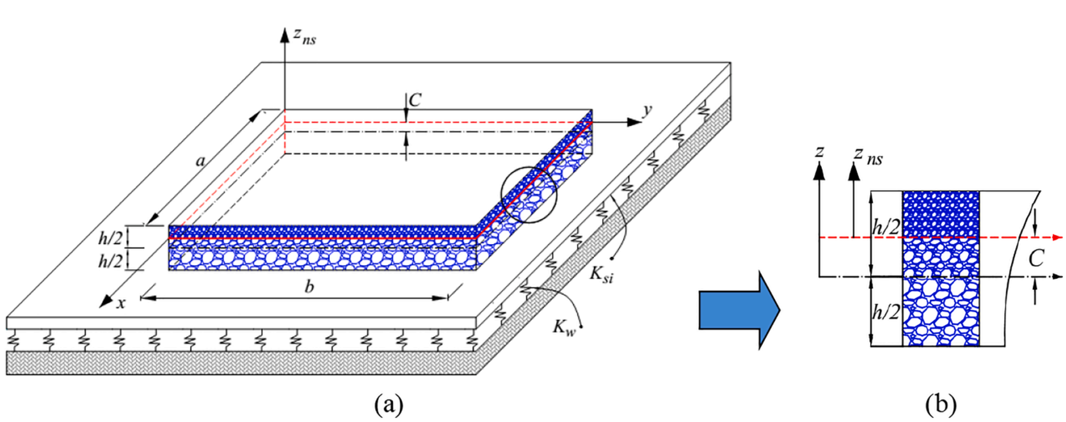

Fig. 1. The geometry and cross-section rectangular FGP plate.

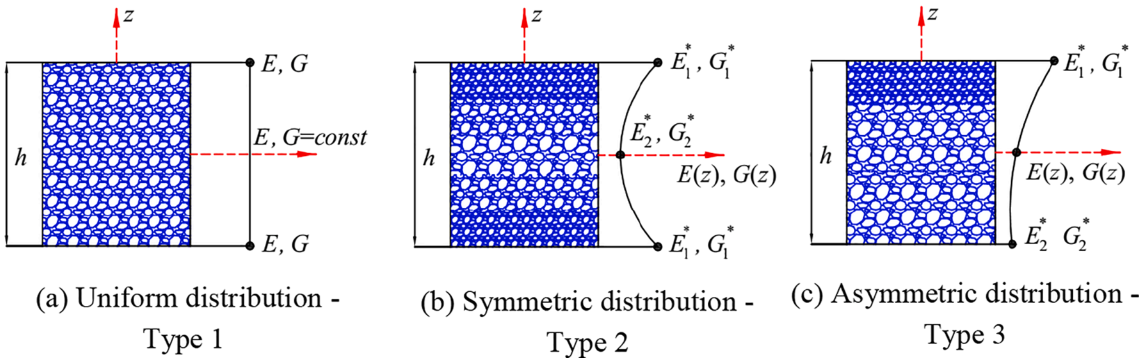

Fig. 2. The FGP plate with different porosity density distribution patterns.

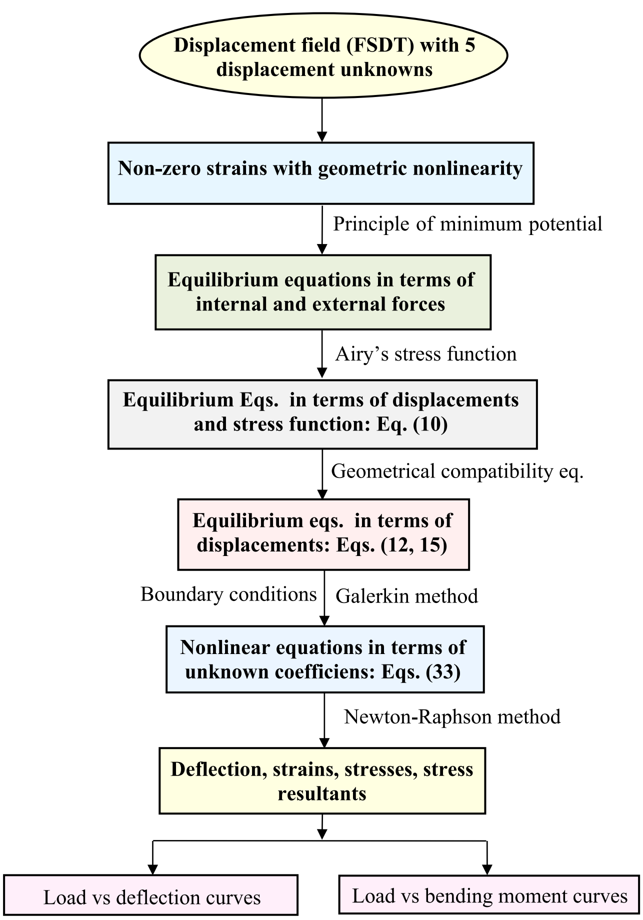

Fig. 3. The flowchart of nonlinear bending analysis of FGP plates.

3. Theoretical model

3.1. Basic equations based on the physical neutral position concept

Based on FSDT, applying the neutral surface position concept as shown in Fig. 3, the displacement components $\overline{u}$, $\overline{v}$, $\overline{w}$ at an arbitrary point $(x,\ y,\ z_{ns})$ along x, y and z axes of the FGP plate are expressed as follows [40]:

$$\begin{aligned}\overline{u}(x,y,\ z_{ns}) &= \overline{u}_0(x,y) + z_{ns}\overline{\theta}_x(x,y);\\ \overline{v}(x,\ y,\ z_{ns}) &= \overline{v}_0(x,y) + z_{ns}\overline{\theta}_y(x,y);\\ \overline{w}(x,\ y,\ z_{ns}) &= \overline{w}_0(x,y)\end{aligned} \tag{6}$$

where: $\overline{u}_0, \overline{v}_0, \overline{w}_0$ are the neutral-plane displacements in the x, y, and z directions; $\overline{\theta}_x, \overline{\theta}_y$ are rotations of transverse normal about the y and x axes, respectively.

Strain components include the von Kármán geometric nonlinearity are defined as:

$$\begin{Bmatrix}\varepsilon_x\\ \varepsilon_y\\ \gamma_{xy}\end{Bmatrix} = \begin{Bmatrix}\varepsilon_x^0\\ \varepsilon_y^0\\ \gamma_{xy}^0\end{Bmatrix} + z_{ns}\begin{Bmatrix}k_x\\ k_y\\ k_{xy}\end{Bmatrix};\ \begin{Bmatrix}\gamma_{xz}\\ \gamma_{yz}\end{Bmatrix} = \begin{Bmatrix}\gamma_{xz}^0\\ \gamma_{yz}^0\end{Bmatrix} \tag{7}$$

in which: $\varepsilon_x^0 = \overline{u}_{0,x} + \frac{1}{2}\overline{w}_{0,x}^2;\ \varepsilon_y^0 = \overline{v}_{0,y} + \frac{1}{2}\overline{w}_{0,y}^2;\ \gamma_{xy}^0 = \overline{u}_{0,y} + \overline{v}_{0,x} + \overline{w}_{0,x}\overline{w}_{0,y};\ k_x = \overline{\theta}_{x,x};$ $k_y = \overline{\theta}_{y,y};\ k_{xy} = \overline{\theta}_{x,y} + \overline{\theta}_{y,x};\ \gamma_{xz}^0 = \overline{w}_{0,x} + \overline{\theta}_x;\ \gamma_{yz}^0 = \overline{w}_{0,y} + \overline{\theta}_y$.

The commas subscript denote the partial differentiation with respect to the spatial variables.

Stresses are determined from Hooke's law and written as:

$$\begin{Bmatrix}\overline{\sigma}_x\\ \overline{\sigma}_y\\ \overline{\sigma}_{xy}\end{Bmatrix} = \begin{bmatrix}\widetilde{Q}_{11} & \widetilde{Q}_{12} & 0\\ \widetilde{Q}_{21} & \widetilde{Q}_{22} & 0\\ 0 & 0 & \widetilde{Q}_{66}\end{bmatrix}\begin{Bmatrix}\varepsilon_x\\ \varepsilon_y\\ \gamma_{xy}\end{Bmatrix};\ \begin{Bmatrix}\overline{\sigma}_{xz}\\ \overline{\sigma}_{yz}\end{Bmatrix} = \begin{bmatrix}\widetilde{Q}_{55} & 0\\ 0 & \widetilde{Q}_{44}\end{bmatrix}\begin{Bmatrix}\gamma_{xz}\\ \gamma_{yz}\end{Bmatrix} \tag{8}$$

where: $\widetilde{Q}_{11} = \widetilde{Q}_{22} = \frac{E(z_{ns})}{1-\nu^2};\widetilde{Q}_{12} = \widetilde{Q}_{21} = \frac{\nu E(z_{ns})}{1-\nu^2};\ \widetilde{Q}_{44} = \widetilde{Q}_{55} = \widetilde{Q}_{66} = \frac{E(z_{ns})}{2(1+\nu)}$.

The stress resultants of a plate are obtained in the form:

$$\begin{Bmatrix}N_x\\ N_y\\ N_{xy}\end{Bmatrix} = \begin{bmatrix}A_{11} & A_{12} & 0\\ A_{12} & A_{11} & 0\\ 0 & 0 & A_{66}\end{bmatrix}\begin{Bmatrix}\varepsilon_x^0\\ \varepsilon_y^0\\ \gamma_{xy}^0\end{Bmatrix};\ \begin{Bmatrix}M_x\\ M_y\\ M_{xy}\end{Bmatrix} = \begin{bmatrix}C_{11} & C_{12} & 0\\ C_{12} & C_{11} & 0\\ 0 & 0 & C_{66}\end{bmatrix}\begin{Bmatrix}k_x\\ k_y\\ k_{xy}\end{Bmatrix};\ \begin{Bmatrix}Q_{xz}\\ Q_{yz}\end{Bmatrix} = \begin{bmatrix}A_{44}^s & 0\\ 0 & A_{44}^s\end{bmatrix}\begin{Bmatrix}\gamma_{xz}^0\\ \gamma_{yz}^0\end{Bmatrix} \tag{9}$$

where: $(A_{ij}, C_{ij}) = \int_{-h/2-C}^{h/2-C} Q_{ij}\left(1, \bar{z}_{ns}^2\right) d\bar{z}_{ns}$; $ij = 11, 12, 66$; and the shear correction factor $k_s = 5/6$ is employed in this study.

The equilibrium equations are derived by using the principle of minimum potential energy, and are expressed as bellow [40,41]:

$$N_{x,x} + N_{xy,y} = 0;\ N_{y,y} + N_{xy,x} = 0;\ N_x.\overline{w}_{0,xx} + 2N_{xy}.\overline{w}_{0,xy} + N_y.\overline{w}_{0,yy} + Q_{xz,x} + Q_{yz,y} + q_f + q = 0;\ M_{x,x} + M_{xy,y} - Q_{xz} = 0;\ M_{y,y} + M_{xy,x} - Q_{yz} = 0 \tag{10}$$

in which: $q_f = -K_w\overline{w}_0 + K_{sx}\overline{w}_{0,xx} + K_{sy}\overline{w}_{0,yy}$.

Using Airy stress function $\varphi(x, y)$ defined by:

$$N_x = \varphi_{,yy};\quad N_y = \varphi_{,xx};\quad N_{xy} = -\varphi_{,xy} \tag{11}$$

It is seen that the first two equations in Eqs. (10) are automatically satisfied.

Applying the relationship of Eqs. (7), (9) and (11), the three rest equations are re-written in terms of the displacements and stress function as follows:

$$A_{44}^s\left(\overline{w}_{0,xx} + \overline{w}_{0,yy} + \overline{\theta}_{x,x} + \overline{\theta}_{y,y}\right) + \varphi_{,yy}\overline{w}_{0,xx} - 2\varphi_{,xy}\overline{w}_{0,xy} + \varphi_{,xx}\overline{w}_{0,yy} + q_f + q = 0;\ C_{11}\overline{\theta}_{x,xx} + C_{66}\overline{\theta}_{x,yy} + (C_{12} + C_{66})\overline{\theta}_{y,xy} - A_{44}^s\left(\overline{\theta}_x + \overline{w}_{0,x}\right) = 0;\ C_{11}\overline{\theta}_{y,yy} + C_{66}\overline{\theta}_{y,xx} + (C_{12} + C_{66})\overline{\theta}_{x,xy} - A_{44}^s\left(\overline{\theta}_y + \overline{w}_{0,y}\right) = 0 \tag{12}$$

Meanwhile, the geometrical compatibility equation for the rectangular plate is expressed as [42]:

$$\varepsilon_{x,yy}^0 + \varepsilon_{y,xx}^0 - \gamma_{xy,xy}^0 = \overline{w}_{0,xy}^2 - \overline{w}_{0,xx}\overline{w}_{0,yy} \tag{13}$$

Based on the Eqs. (9) and (11), the in-plane strains are determined in terms of in-plane stress resultants and stress function:

$$\varepsilon_x^0 = c_{11}N_x - c_{12}N_y = c_{11}\varphi_{,yy} - c_{12}\varphi_{,xx};$$

$$\varepsilon_y^0 = c_{11}N_y - c_{12}N_x = c_{11}\varphi_{,xx} - c_{12}\varphi_{,yy};$$

$$\gamma_{xy}^0 = c_{66}N_{xy} = -c_{66}\varphi_{,xy} \tag{14}$$

in which: $c_{11} = \frac{A_{11}}{A_{11}^2 - A_{12}^2}$; $c_{12} = \frac{A_{12}}{A_{11}^2 - A_{12}^2}$; $c_{66} = \frac{1}{A_{66}}$.

Substituting Eq. (14) into the compatibility equation Eq. (13), we have:

$$\nabla^4\varphi = D\left[\left(\frac{\partial^2\overline{w}_0}{\partial x\partial y}\right)^2 - \frac{\partial^2\overline{w}_0}{\partial x^2}\frac{\partial^2\overline{w}_0}{\partial y^2}\right] \tag{15}$$

where: $\nabla^4 = \frac{\partial^4}{\partial x^4} + \frac{\partial^4}{\partial y^4} + 2\frac{\partial^4}{\partial x^2\partial y^2}$; $D = A_{11}\left(1 - \nu^2\right)$.

The system consisting of three equations in Eqs. (12) and Eq. (15) are the governing equations used to investigate the nonlinear bending behavior of FGP plates. This is a system of four nonlinear equations with 4 independent unknowns.

3.2. Nonlinear bending analysis

In this section, based on the Bubnov-Galerkin method, analytical solutions for nonlinear bending analysis of FGP rectangular plate under six cases of boundary conditions (BCs) are proposed.

Case 1: All four edges of plates are simply supported and freely movable in both the x and y directions and referred to as SSSS-FM. The associated BCs are:

$$\overline{w}_0 = \overline{\theta}_s = 0,\ N_{ns} = 0, M_n = 0, N_n = N_{n0} = 0 \tag{16}$$

Case 2: All four edges of plates are simply supported and immovable and referred to as SSSS-IM. The associated BCs are:

$$\overline{u}_n = \overline{w}_0 = \overline{\theta}_s = 0,\ N_{ns} = 0, M_n = 0 \tag{17}$$

Case 3: All four edges of plates are clamped and freely movable in both the x and y directions and referred to as CCCC-FM. The associated BCs are:

$$\overline{w}_0 = \overline{\theta}_n = \overline{\theta}_s = 0,\ N_{ns} = 0, N_n = N_{n0} = 0 \tag{18}$$

Case 4: All four edges of plates are clamped and immovable and referred to as CCCC-IM. The associated BCs are:

$$\overline{u}_n = \overline{w}_0 = \overline{\theta}_n = \overline{\theta}_s = 0,\ N_{ns} = 0 \tag{19}$$

Case 5: Two opposite edges are simply supported, the others are clamped and freely movable and referred to as SCSC-FM. The associated BCs are:

$$\text{At}\,x = 0, a:\ \overline{w}_0 = \overline{\theta}_y = 0; M_x = 0; N_x = N_{x0} = 0;$$
$$\text{At}\,y = 0, b\ \overline{w}_0 = \overline{\theta}_x = \overline{\theta}_y = 0; N_{xy} = 0; N_y = N_{y0} = 0$$

Case 6: Two opposite edges are simply supported, the others are clamped and immovable and referred to as SCSC-IM. The associated BCs are:

$$\text{At}\,x = 0, a:\ \overline{u}_0 = \overline{w}_0 = \overline{\theta}_y = 0; N_{xy} = 0; M_x = 0;$$
$$\text{At}\,y = 0, b:\ \overline{v}_0 = \overline{w}_0 = \overline{\theta}_x = \overline{\theta}_y = 0; N_{xy} = 0$$

in which: N_{x0}, N_{y0} are in-plane compressive loads at movable edges of the rectangular plate and are fictitious compressive edge loads at immovable edges.

The in-plane imovable BCs, such as $\overline{u}_0 = 0$ (at $x = 0, a$) and $\overline{v}_0 = 0$ (at $y = 0, b$) are satisfied on the average sense [43]:

$$\int_0^b\int_0^a \overline{u}_{0,x}dxdy = 0;\quad \int_0^b\int_0^a \overline{v}_{0,y}dxdy = 0 \tag{22}$$

In general, for all the above-mentioned BCs, the stress function is chosen in the form as below:

$$\varphi = \overline{\varphi}(x, y) + N_{x0}\frac{y^2}{2} + N_{y0}\frac{x^2}{2} \tag{23}$$

in which, for moveable in-plane BCs:

$$N_{x0} = \frac{1}{b}\int_0^b \widehat{N}_x dy = 0;\quad N_{y0} = \frac{1}{a}\int_0^a \widehat{N}_y dx = 0 \tag{24}$$

and for immoveable BCs, from Eq. (22) we obtain in-plane support reactions as follows:

$$N_{x0} = \frac{1}{ab}\int_0^b\int_0^a\left(-\overline{\varphi}_{,yy} + \frac{A_{11}\overline{w}_{0,x}^2}{2} + \frac{A_{12}\overline{w}_{0,y}^2}{2}\right)dxdy;$$

$$N_{y0} = \frac{1}{ab}\int_0^b\int_0^a\left(-\overline{\varphi}_{,xx} + \frac{A_{12}\overline{w}_{0,x}^2}{2} + \frac{A_{11}\overline{w}_{0,y}^2}{2}\right)dxdy \quad (25)$$

With the BCs: SSSS-FM and SSSS-IM, the displacement solutions are assumed as follows:

$$\overline{w}_0 = \sum_{m=1}^{\infty}\sum_{n=1}^{\infty}\overline{w}_{0mn}sin\lambda_m x sin\delta_n y;$$
$$\overline{\theta}_x = \sum_{m=1}^{\infty}\sum_{n=1}^{\infty}\overline{\theta}_{xmn}cos\lambda_m x sin\delta_n y; \quad (26)$$
$$\overline{\theta}_y = \sum_{m=1}^{\infty}\sum_{n=1}^{\infty}\overline{\theta}_{ymn}sin\lambda_m x cos\delta_n y$$

where: $\lambda_m = \frac{m\pi}{a}, \delta_n = \frac{n\pi}{b}$; m, n are odd integers and $\overline{w}_{0mn}, \overline{\theta}_{xmn}, \overline{\theta}_{ymn}$ are unknown coefficients to be determined.

Substituting Eq. (26) into Eq. (15), we obtain:

$$\overline{\varphi} = \sum_p\sum_q\sum_r\sum_s \overline{w}_{0pq}\overline{w}_{0rs}H_{pqrs}^{(1)}(x,y) \quad (27)$$

where $H_{pqrs}^{(1)}(x,y)$ are presented in Appendix 1.

With the BCs: CCCC-FM and CCCC-IM, the displacement solutions are chosen as below:

$$\overline{w}_0 = \sum_{m=1}^{\infty}\sum_{n=1}^{\infty}\overline{w}_{0mn}sin^2\lambda_m x sin^2\delta_n y;$$
$$\overline{\theta}_x = \sum_{m=1}^{\infty}\sum_{n=1}^{\infty}\overline{\theta}_{xmn}sin2\lambda_m x sin^2\delta_n y; \quad (28)$$
$$\overline{\theta}_y = \sum_{m=1}^{\infty}\sum_{n=1}^{\infty}\overline{\theta}_{ymn}sin^2\lambda_m x sin2\delta_n y$$

$$\sum_m\sum_n\left(\overline{w}_{0mn}l_{mn}^{(33)} + \overline{\theta}_{xmn}l_{mn}^{(34)} + \overline{\theta}_{ymn}l_{mn}^{(35)}\right) + \sum_m\sum_n\sum_p\sum_q\sum_r\sum_s\overline{w}_{0mn}\overline{w}_{0pq}\overline{w}_{0rs}g_{mnpqrs}^{(33)} + q = 0;$$

Substituting Eq. (28) into Eq. (15), we obtain:

$$\overline{\varphi} = \sum_p\sum_q\sum_r\sum_s \overline{w}_{0pq}\overline{w}_{0rs}H_{pqrs}^{(2)}(x,y) \quad (29)$$

where $H_{pqrs}^{(2)}(x,y)$ are presented in Appendix 2.

With the BCs: SCSC-FM and SCSC-IM, the displacement solutions are chosen as below:

Table 1
The non-dimensional central deflection $\overline{w}$ of the simply supported isotropic square plate (SSSS-FM, SSSS-IM) under uniformly distributed load.

P	Kapoor and Kapania [44]	Present			
		$m, n = 1$	$m, n = 2$	$m, n = 3$	$m, n = 4$
	SSSS-FM				
6.25	0.284	0.2911	0.2819	0.2829	0.2826
12.5	0.5244	0.5424	0.5236	0.5257	0.5252
25	0.879	0.9196	0.8804	0.8848	0.8838
50	1.3341	1.4034	1.3221	1.3319	1.3299
100	1.8918	1.9841	1.8230	1.8450	1.8409
	SSSS-IM				
6.25	0.2784	0.2720	0.2627	0.2637	0.2635
12.5	0.4626	0.4624	0.4434	0.4455	0.4450
25	0.691	0.7075	0.6681	0.6727	0.6716
50	0.9579	1.0018	0.9209	0.9315	0.9295
100	1.2696	1.3533	1.1907	1.2166	1.2125

$$\overline{w}_0 = \sum_{m=1}^{\infty}\sum_{n=1}^{\infty}\overline{w}_{0mn}sin\alpha_m x sin^2\delta_n y;$$
$$\overline{\theta}_x = \sum_{m=1}^{\infty}\sum_{n=1}^{\infty}\overline{\theta}_{xmn}cos\alpha_m x sin^2\delta_n y; \quad (30)$$
$$\overline{\theta}_y = \sum_{m=1}^{\infty}\sum_{n=1}^{\infty}\overline{\theta}_{ymn}sin\alpha_m x sin2\delta_n y$$

Substituting Eq. (30) into Eq. (15), we obtain:

$$\overline{\varphi} = \sum_p\sum_q\sum_r\sum_s \overline{w}_{0pq}\overline{w}_{0rs}H_{pqrs}^{(3)}(x,y) \quad (31)$$

where $H_{pqrs}^{(3)}(x,y)$ are presented in Appendix 3.

After finding $\overline{\varphi}$ from (27), (29) and (31), the in-plane forces N_{x0}, N_{y0} can be derived from Eq. (25) for particular boundary conditions.

Finally, obtained $\overline{\varphi}$ and N_{x0}, N_{y0} are substituted into Eq. (23) to get the stress function $\varphi(x,y)$; then substituting into Eqs. (12), the new set of equations in terms $\overline{w}_0, \overline{\theta}_x, \overline{\theta}_y$ are expressed as:

$$\sum_m\sum_n\left(\overline{w}_{0mn}l_{mn}^{(43)} + \overline{\theta}_{xmn}l_{mn}^{(44)} + \overline{\theta}_{ymn}l_{mn}^{(45)}\right) = 0;$$

$$\sum_m\sum_n\left(\overline{w}_{0mn}l_{mn}^{(53)} + \overline{\theta}_{xmn}l_{mn}^{(54)} + \overline{\theta}_{ymn}l_{mn}^{(55)}\right) = 0 \quad (32)$$

Applying the Galerkin method Eqs. (32) become:

$$\sum_m\sum_n\left(\overline{w}_{0mn}L_{mnij}^{(33)} + \overline{\theta}_{xmn}L_{mnij}^{(34)} + \overline{\theta}_{ymn}L_{mnij}^{(35)}\right) + \sum_m\sum_n\sum_p\sum_q\sum_r\sum_s\overline{w}_{0mn}\overline{w}_{0pq}\overline{w}_{0rs}G_{mnpqrsij}^{(33)} + F_{ij} = 0;$$

Table 2
The non-dimensional central deflection $\overline{w}$ of isotropic square plate (SCSC-IM) under uniformly distributed load.

P	Azizian and Dawe [46]	Lei [45]	Present			
			$m, n =$ 1	$m, n =$ 2	$m, n =$ 3	$m, n =$ 4
0.9158	0.0199	0.0199	0.0199	0.0193	0.0198	0.0197
4.5788	0.0988	0.0984	0.0992	0.0960	0.0982	0.0981
6.8681	0.1469	0.1455	0.1477	0.1429	0.1461	0.1461
9.1575	0.1936	0.1904	0.1950	0.1886	0.1929	0.1927

Table 3
Nondimensional central deflection $\overline{w}$ of square FGP plate under uniform loading.

P	SSSS-FM	SCSC-FM	CCCC-FM	SSSS-IM	SCSC-IM	CCCC-IM
1	0.0732	0.0352	0.0234	0.0728	0.0352	0.0234
2	0.1456	0.0704	0.0469	0.1424	0.0702	0.0469
5	0.3505	0.1754	0.1169	0.3178	0.1726	0.1166
10	0.6352	0.3464	0.2319	0.5173	0.3278	0.2298
15	0.8562	0.5097	0.3433	0.6537	0.4604	0.3370
20	1.0330	0.6634	0.4501	0.7575	0.5729	0.4369
25	1.1796	0.8067	0.5515	0.8416	0.6695	0.5292
30	1.3049	0.9399	0.6474	0.9126	0.7540	0.6142

Table 4
Bending moment M_x [MNm/m] of square FGP plate under uniform loading.

P	SSSS-FM	SCSC-FM	CCCC-FM	SSSS-IM	SCSC-IM	CCCC-IM
1	0.2467	0.1325	0.1289	0.2452	0.1324	0.1289
2	0.4899	0.2649	0.2576	0.4783	0.2641	0.2575
5	1.1697	0.6593	0.6420	1.0529	0.6477	0.6403
10	2.0716	1.2991	1.2697	1.6645	1.2229	1.2571
15	2.7186	1.9045	1.8712	2.0441	1.7043	1.8332
20	3.1930	2.4674	2.4385	2.3057	2.1039	2.3602
25	3.5532	2.9853	2.9674	2.4975	2.4401	2.8369
30	3.8355	3.4598	3.4572	2.6439	2.7283	3.2663

$$\sum_m\sum_n\left(\overline{w}_{0mn}L^{(43)}_{mnij}+\overline{\theta}_{xmn}L^{(44)}_{mnij}+\overline{\theta}_{ymn}L^{(45)}_{mnij}\right)=0;$$
$$\sum_m\sum_n\left(\overline{w}_{0mn}L^{(53)}_{mnij}+\overline{\theta}_{xmn}L^{(54)}_{mnij}+\overline{\theta}_{ymn}L^{(55)}_{mnij}\right)=0 \quad (33)$$

By using the Newton-Raphson interactive method to solve the Eqs. (33), the displacement vector $\left\{\overline{w}_{0mn};\overline{\theta}_{xmn};\overline{\theta}_{ymn}\right\}$ is obtained to get displacements, and then strains, stresses, internal force resultants are derived to investigate static nonlinear bending of FGP plates. The flowchart illustrates the solution procedure is shown in Fig. 3.

4. Results and discussion

With the analytical solution set up above, the program in Matlab is used to practice the numerical examples. The analyzing results are nonlinear except for the mentioned cases. Dimensionless formulas are used [28,29]:

$$\overline{w}=\frac{1}{h}\overline{w}_0\left(\frac{a}{2},\frac{b}{2}\right);\ K_0=\frac{K_wa^4}{E^*h^3};\ J_0=\frac{K_{sx}a^2}{E^*h^3\nu}=\frac{K_{sy}b^2}{E^*h^3\nu};\ E^*=1.0\,\text{GPa};\ P=\frac{q_0a^4}{E_1h^4} \quad (34)$$

4.1. Validation

To obtain a reasonable accuracy and validate the present approach, the non-dimensional central deflections of the homogeneous isotropic square plate are calculated by increasing the number of terms (m, n) in the expansion of the trigonometric series. Table 1 presents the numerical results for simply supported boundary conditions (SSSS-FM, SSSS-IM) with input data: $E = 7.8\times10^6$ psi; $\nu = 0.3$; $h = 1$ in.; $a = b = 10\ h$. The comparison is made with those of Kapoor and Kapania [44] applying the isogeometric element method incorporated with FSDT.

Table 2 shows the non-dimensional central deflections of the isotropic square plate ($h/a = 0.05$; $\nu = 0.3$; $E = 0.3\times10^7$psi) with SCSC-IM boundary conditions subjected to uniformly distributed load. The present results are compared with those of Lei [45] using the boundary element method in conjunction with FSDT, and Azizian and Dawe [46] applying the finite strip method based on FSDT.

As can be seen from Tables 1 and 2, the increasing number of expanded terms improves the accuracy of results which converge at $m = n = 3$. Thus, in all next calculations, $m = n = 3$ is used for simplicity. Besides, two comparisons also show that the obtained results match well with available ones, and thus the validity can be confirmed.

4.2. Nonlinear analysis

Considering the FGP (metal foam) rectangular plate ($h = 0.1$ m, $E_1 =$ 200GPa, $\nu = 1/3$) rested on the elastic foundation, under the uniformly distributed load P.

Tables 3 and 4 present the nondimensional central deflection and bending moment M_x [Nm/m] of square FGP plate ($a/h = 20$, $b/a = 1$, Type 3, $e_0 = 0.6$, $K_0 = J_0 = 0$) under various boundary conditions and subjected to increased uniform loads.

Figs. 4 and 5 show the nonlinear variation of central displacement

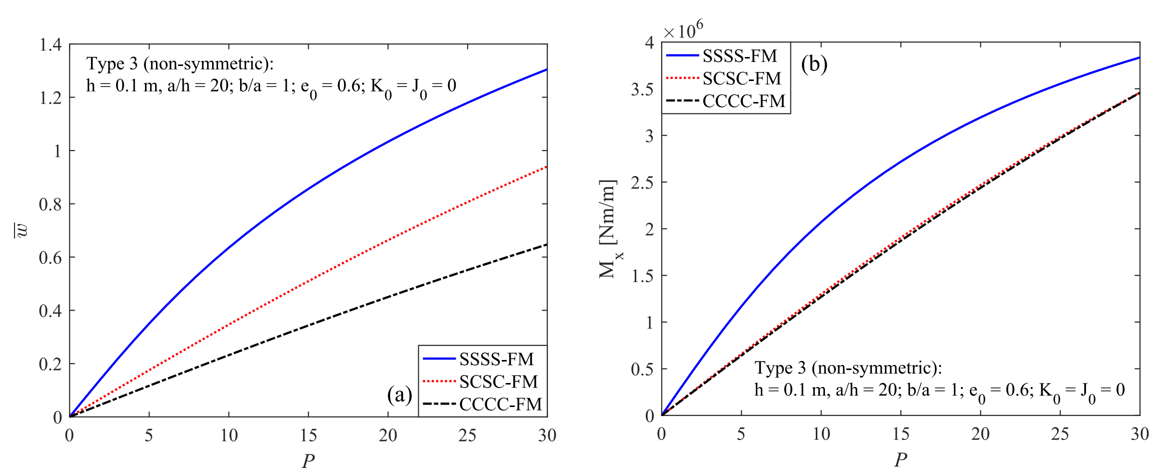

Fig. 4. Nonlinear bending response of FGP plates under various freely moveable boundary conditions: (a) Load vs deflection curves, (b) Load vs bending moment curves.

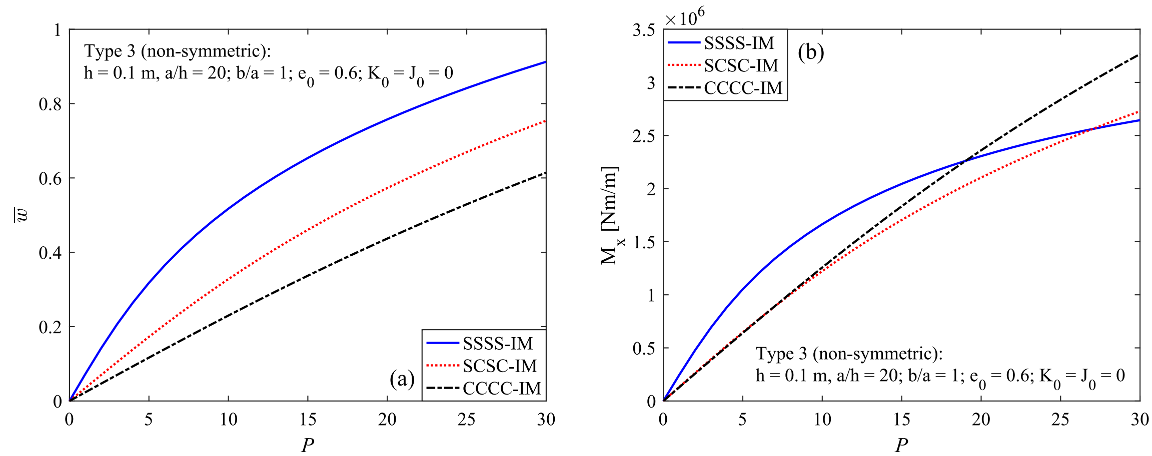

Fig. 5. Nonlinear bending response of FGP plates under various immoveable boundary conditions: (*a*) Load vs deflection curves, (*b*) Load vs bending moment curves.

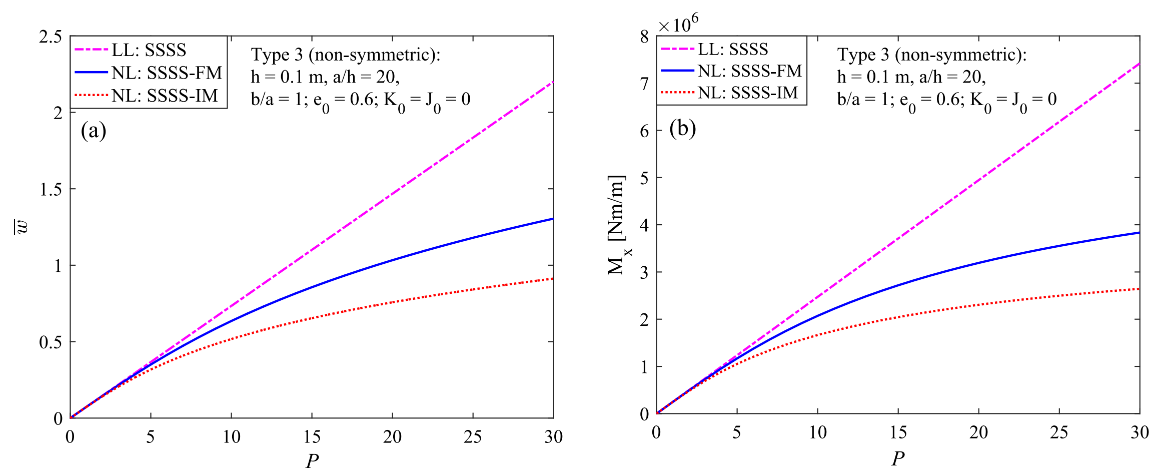

Fig. 6. Effect of in-plane constraints on linear (LL) and nonlinear (NL) bending behavior of SSSS square FGP plates: (*a*) Load vs deflection curves, (*b*) Load vs bending moment curves.

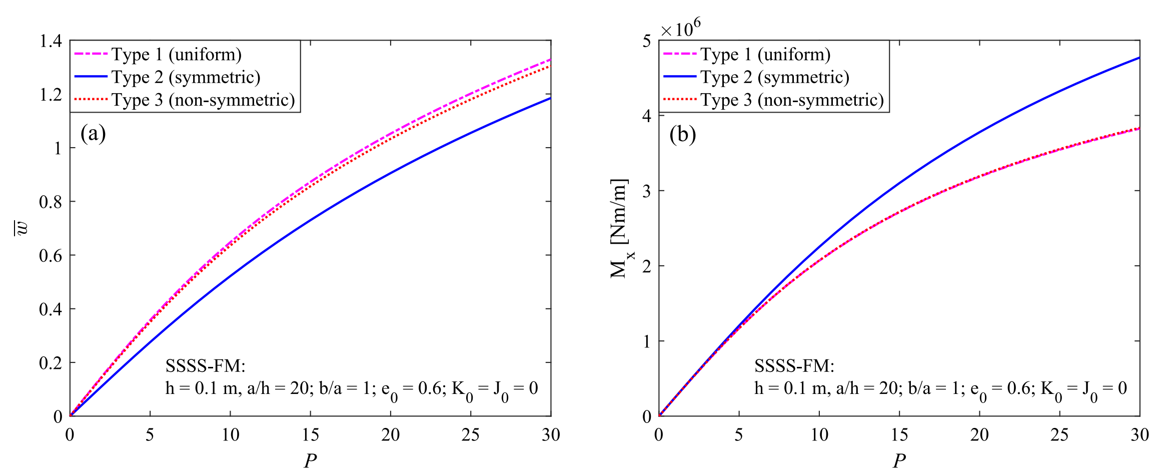

Fig. 7. Effect of porosity distribution patterns on the nonlinear bending response of FGP square plates: (*a*) Load vs deflection curves, (*b*) Load vs bending moment curves.

and bending moment versus increased load for various freely moveable (immoveable) boundary conditions respectively. It is observed that deflection in both moveable and immoveable SSSS are greater than those under the remaining two types of boundary conditions. Results also indicate that the plate with movable edges produces much more deflection than the plate with immoveable edges. The law of variation of bending moment is more complicated depending on the values of applied loading and in-plane constraints.

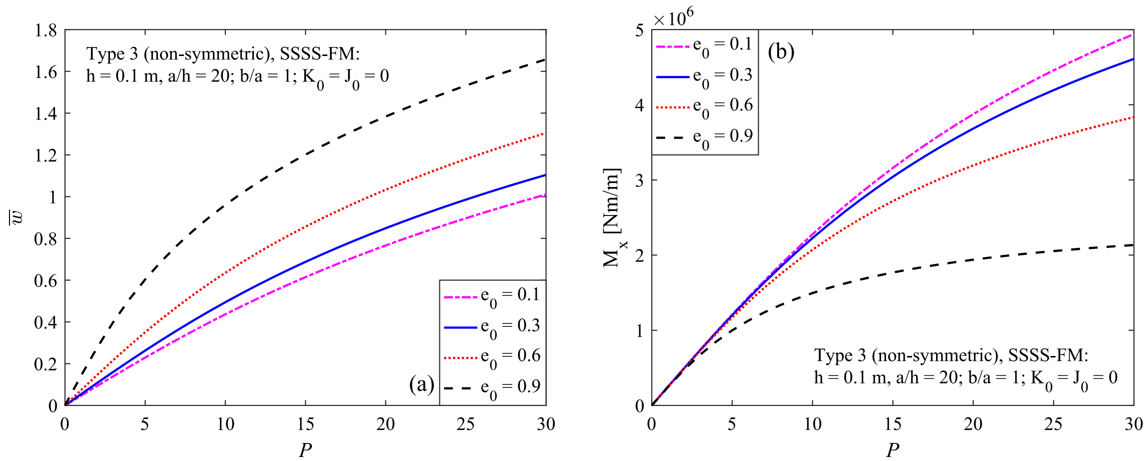

Fig. 8. Effect of porosity coefficient on the nonlinear bending response of FGP square plates: (*a*) Load vs deflection curves, (*b*) Load vs bending moment curves.

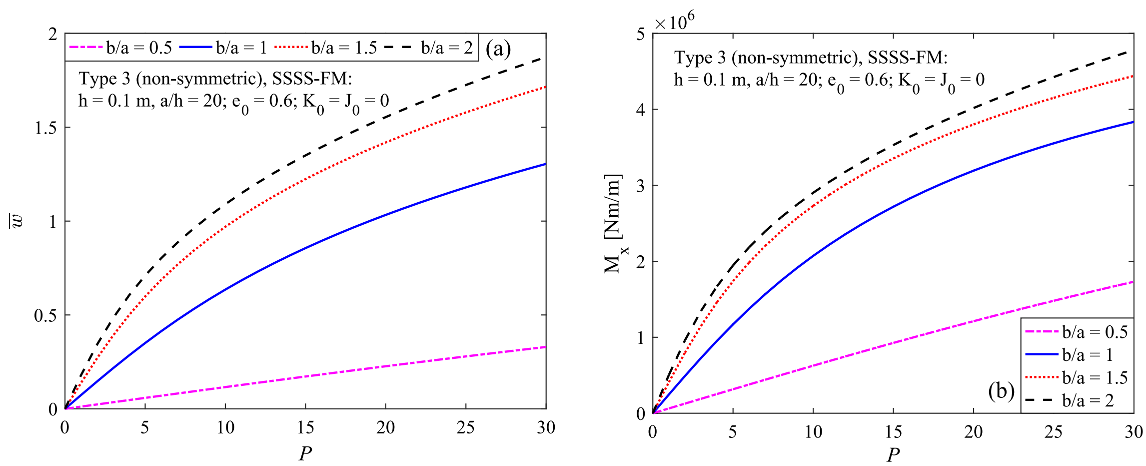

Fig. 9. Effect of aspect ratio (b/a) on the nonlinear bending response of FGP ($a/h = 20$) plates: (*a*) Load vs deflection curves, (*b*) Load vs bending moment curves.

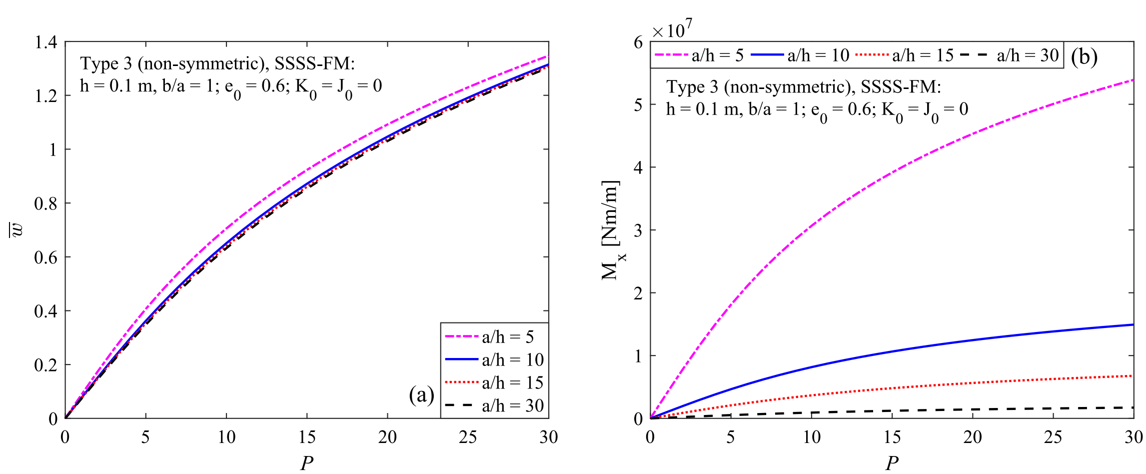

Fig. 10. Effect of length-to-thickness ratio (a/h) on the nonlinear bending response of square FGP plates: (*a*) Load vs deflection curves, (*b*) Load vs bending moment curves.

Fig. 6 depicts the influence of in-plane boundary conditions on the linear and nonlinear behavior FGP square plates (SSSS, $a/h = 20$, $b/a = 1$, $e_0 = 0.6$, $K_0 = J_0 = 0$) subjected to uniform transverse loading. As expected, it is seen that the results obtained by linear analysis are always higher than by nonlinear analysis, and higher applied load causes a bigger gap between two approaches. Linear bending behavior for both moveable and immoveable is the same, while according to nonlinear analysis the load–deflection and load-bending moment curves of FGP plates under moveable boundary conditions are always higher than those under immoveable boundary conditions.

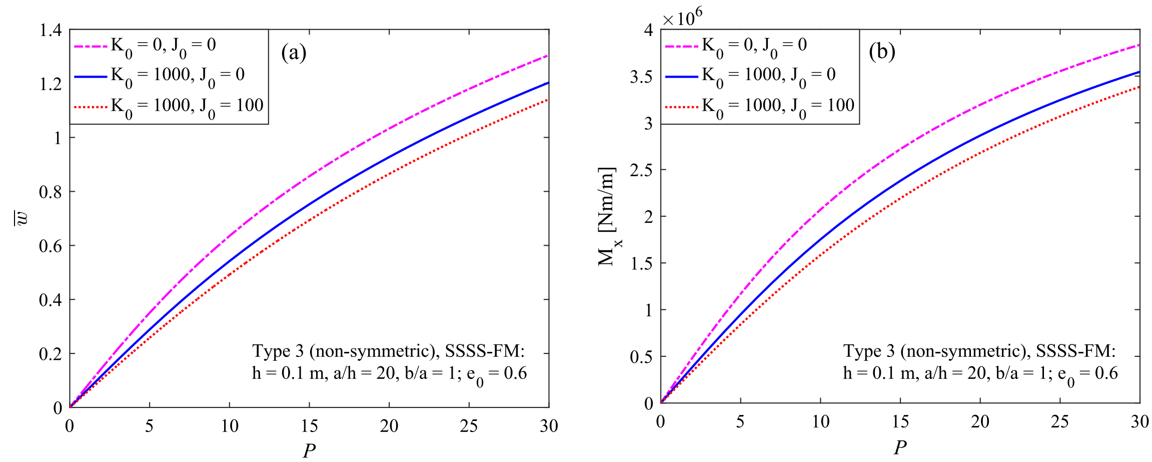

Fig. 11. Effect of elastic foundations on the nonlinear bending response of square FGP plates: (*a*) Load vs deflection curves, (*b*) Load vs bending moment curves.

The nonlinear bending response of SSSS-FM (freely moveable simply supported) FGP plates with three porosity distribution patterns is plotted in Fig. 7. This figure indicates that the deflection

with symmetric porosity distribution (Type 2) is the smallest, but the bending moment is the highest. There is a slight discrepancy of obtained results between uniform porosity distribution (Type 1) and non-symmetric porosity distribution (Type 3).

The influence of porosity coefficient on nonlinear bending response of SSSS-FM square FGP (Type 3) plate is illustrated in Fig. 8. It can be seen that at the given applied load, the central nondimensional deflection gets bigger as the porosity coefficient increases and this trend is opposite to the bending moment. This is because the increasing porosity coefficient increases the size and amount of internal pores which results in a decrease of the FGP plate stiffness. Furthermore, the larger the porosity coefficient, the greater load–deflection nonlinearity.

Figs. 9 and 10 present the effect of aspect ratio b/a and length-to-thickness ratio a/h on nonlinear bending behaviors of FGP plates (SSSS-FM, $e_0 = 0.6$, $K_0 = J_0 = 0$). The plots show that the nondimensional central displacement and bending moment increase as the b/a ratio increases. This can be explained by the fact that a large plate more easily deforms under bending.

Observing Fig. 10 we can see that the load-bending moment curve is significantly sensitive to the a/h ratio, while the load–deflection curve is only slightly sensitive. Furthermore, as the a/h ratio increases, both nondimensional central deflection and bending moment decrease.

Fig. 11 illustrates the effect of various types of elastic foundation ($K_0 = 1000$, $J_0 = 100$ for Pasternak's foundation; $K_0 = 1000$, $J_0 = 0$ for Winkler's foundation; and $K_0 = J_0 = 0$ for plate without foundation) on the load–deflection and load-bending moment curves. It appears that the elastic foundation significantly influences the nonlinear bending behavior of FGP plates. The deflections, as well as bending moment of the plates resting on Winkler's elastic foundation are between those of foundationless plates and the plates resting on Pasternak elastic foundation.

5. Conclusion

Based on the first-order shear deformation theory, the nonlinear bending behavior of the FGP plate resting on the elastic foundation subjected to uniformly transverse distributed loading is investigated. Using stress function in conjunction with the Galerkin method, the analytical solutions are derived to determine the load–deflection and load–bending moment curves for various edges boundary conditions. Three porosity distribution patterns with varied porosity coefficients are considered. After convergence and validation study, parametric studies have been performed to study the influence of geometrical parameters (b/a and a/h ratios), material parameters (porosity distribution patterns, porosity coefficients), boundary conditions and elastic foundations on nonlinear bending behavior of FGP plates. Major findings are listed as follows:

- By introducing the physical neutral surface concept, the stretching-bending coupling effect is eliminated, the governing equations for analyzing nonlinear bending response in the simple form are obtained.
- The solution of governing equations for nonlinear bending problems have been carried out by using m and n terms in Fourier's series expansion. The number of terms $m = n = 3$ is chosen for the sake of convenience, which is enough for convergence.
- The deflection with symmetric porosity distribution is the smallest, but the bending moment is the highest. There is a slight discrepancy of obtained results between uniform porosity distribution and non-symmetric porosity distribution.
- The nonlinear deflections are smaller than linear deflections. The larger the porosity coefficient, the greater the effect on the nonlinear bending behavior of FGP plates.
- Nondimensional central displacement and bending moment increase as the b/a ratio increases, and decrease as the a/h ratio increases.
- A plate with movable edges produces much more deflection with larger bending moments than a plate with immovable edges.
- Boundary conditions and elastic foundation significantly affect the nonlinear bending behavior of FGP plates.

Declaration of Competing Interest

The authors declare that they have no known competing financial interests or personal relationships that could have appeared to influence the work reported in this paper.

Acknowledgements

This research is funded by the National University of Civil Engineering (NUCE) under Grant number: 45-2021/KHXD-TD

Appendix 1:. The coefficients in Eq. (27) for SSSS boundary condition

$$H^{(1)}_{pqrs}(x,y)=\kappa_1 cos(\lambda_p-\lambda_r)xcos(\delta_q-\delta_s)y+\kappa_2 cos(\lambda_p+\lambda_r)xcos(\delta_q+\delta_s)y$$
$$+\kappa_3 cos(\lambda_p-\lambda_r)xcos(\delta_q+\delta_s)y+\kappa_4 cos(\lambda_p+\lambda_r)xcos(\delta_q-\delta_s)y;$$

$$\kappa_1=\frac{\frac{D}{4}\left(\lambda_p\lambda_r\delta_q\delta_s-\lambda_p^2\delta_s^2\right)}{\left[\left(\lambda_p-\lambda_r\right)^2+\left(\delta_q-\delta_s\right)^2\right]^2};\ (\text{when } p=r \text{ and } q=s:\kappa_1\ =0);$$

$$\kappa_2=\frac{\frac{D}{4}\left(\lambda_p\lambda_r\delta_q\delta_s-\lambda_p^2\delta_s^2\right)}{\left[\left(\lambda_p+\lambda_r\right)^2+\left(\delta_q+\delta_s\right)^2\right]^2};\kappa_3=\frac{\frac{D}{4}\left(\lambda_p\lambda_r\delta_q\delta_s+\lambda_p^2\delta_s^2\right)}{\left[\left(\lambda_p-\lambda_r\right)^2+\left(\delta_q+\delta_s\right)^2\right]^2};$$

$$\kappa_4=\frac{\frac{D}{4}\left(\lambda_p\lambda_r\delta_q\delta_s+\lambda_p^2\delta_s^2\right)}{\left[\left(\lambda_p+\lambda_r\right)^2+\left(\delta_q-\delta_s\right)^2\right]^2}$$

Appendix 2:. The coefficients in Eq. (29) for CCCC boundary condition

$$H^{(2)}_{pqrs}(x,y)=\kappa_1 cos2(\lambda_p-\lambda_r)xcos2(\delta_q-\delta_s)y+\kappa_2 cos2(\lambda_p+\lambda_r)xcos2(\delta_q+\delta_s)y$$
$$+\kappa_3 cos2(\lambda_p-\lambda_r)xcos2(\delta_q+\delta_s)y+\kappa_4 cos2(\lambda_p+\lambda_r)xcos2(\delta_q-\delta_s)y$$
$$+\kappa_5 cos2\lambda_p xcos2\delta_s y+\kappa_6 cos2\lambda_p xcos2(\delta_q-\delta_s)y$$
$$+\kappa_7 cos2\lambda_p xcos2(\delta_q+\delta_s)y+\kappa_8 cos2(\lambda_p-\lambda_r)xcos2\delta_s y$$
$$+\kappa_9 cos2(\lambda_p+\lambda_r)xcos2\delta_s y;$$

$$\kappa_1=\frac{\frac{D}{16}\left(\lambda_p\lambda_r\delta_q\delta_s-\alpha_p^2\delta_s^2\right)}{\left[\left(\lambda_p-\lambda_r\right)^2+\left(\delta_q-\delta_s\right)^2\right]^2};\ (\text{when } p=r \text{ and } q=s:\kappa_1\ =0);$$

$$\kappa_2=\frac{\frac{D}{16}\left(\lambda_p\lambda_r\delta_q\delta_s-\lambda_p^2\delta_s^2\right)}{\left[\left(\lambda_p+\lambda_r\right)^2+\left(\delta_q+\delta_s\right)^2\right]^2};\kappa_3=\frac{-\frac{D}{16}\left(\lambda_p\lambda_r\delta_q\delta_s+\lambda_p^2\delta_s^2\right)}{\left[\left(\lambda_p-\lambda_r\right)^2+\left(\delta_q+\delta_s\right)^2\right]^2};$$

$$\kappa_4=\frac{-\frac{D}{16}\left(\lambda_p\lambda_r\delta_q\delta_s+\lambda_p^2\delta_s^2\right)}{\left[\left(\lambda_p+\lambda_r\right)^2+\left(\delta_q-\delta_s\right)^2\right]^2};\kappa_5=\frac{-\frac{D}{4}\lambda_p^2\delta_s^2}{\left(\lambda_p^2+\delta_s^2\right)^2};\kappa_6=\frac{\frac{D}{8}\lambda_p^2\delta_s^2}{\left[\lambda_p^2+\left(\delta_q-\delta_s\right)^2\right]^2};$$

$$\kappa_7=\frac{\frac{D}{8}\lambda_p^2\delta_s^2}{\left[\lambda_p^2+\left(\delta_q+\delta_s\right)^2\right]^2};\kappa_8=\frac{\frac{D}{8}\lambda_p^2\delta_s^2}{\left[\left(\lambda_p-\lambda_r\right)^2+\delta_s^2\right]^2};\kappa_9=\frac{\frac{D}{8}\lambda_p^2\delta_s^2}{\left[\left(\lambda_p+\lambda_r\right)^2+\delta_s^2\right]^2}$$

Appendix 3:. The coefficients in Eq. (31) for SCSC boundary condition

$$H^{(3)}_{pqrs}(x,y)=\kappa_1 cos(\lambda_p-\lambda_r)xcos2(\delta_q-\delta_s)y+\kappa_2 cos(\lambda_p+\lambda_r)xcos2(\delta_q+\delta_s)y$$
$$+\kappa_3 cos(\lambda_p-\lambda_r)xcos2(\delta_q+\delta_s)y+\kappa_4 cos(\lambda_p+\lambda_r)xcos2(\delta_q-\delta_s)y$$
$$+\kappa_5 cos(\lambda_p-\lambda_r)xcos2\delta_s y+\kappa_6 cos(\alpha_p+\alpha_r)xcos2\delta_s y;$$

$$\kappa_1=\frac{\frac{D}{4}\left(\lambda_p\lambda_r\delta_q\delta_s-\lambda_p^2\delta_s^2\right)}{\left[\left(\lambda_p-\lambda_r\right)^2+4\left(\delta_q-\delta_s\right)^2\right]^2};\ (\text{when } p=r \text{ and } q=s:K_1\ =0);$$

$$\kappa_2=\frac{\frac{D}{4}\left[\lambda_p\lambda_r\delta_q\delta_s+\lambda_p^2\delta_s^2\right]}{\left[\left(\lambda_p+\lambda_r\right)^2+4\left(\delta_q+\delta_s\right)^2\right]^2};\kappa_3=\frac{-\frac{D}{4}\left(\lambda_p\lambda_r\delta_q\delta_s+\lambda_p^2\delta_s^2\right)}{\left[\left(\lambda_p-\lambda_r\right)^2+4\left(\delta_q+\delta_s\right)^2\right]^2};$$

$$\kappa_4=\frac{-\frac{D}{4}\left(\lambda_p\lambda_r\delta_q\delta_s-\lambda_p^2\delta_s^2\right)}{\left[\left(\lambda_p+\lambda_r\right)^2+4\left(\delta_q-\delta_s\right)^2\right]^2};\kappa_5=\frac{\frac{D}{2}\lambda_p^2\delta_s^2}{\left[\left(\lambda_p-\lambda_r\right)^2+4\delta_s^2\right]^2};\kappa_6=\frac{-\frac{D}{2}\lambda_p^2\delta_s^2}{\left[\left(\lambda_p+\lambda_r\right)^2+4\delta_s^2\right]^2}$$

References

[1] Lefebvre LP, Banhart J, Dunand DC. Porous metals and metallic foams: current status and recent developments. Adv Eng Mater 2008;10(9):775–87.
[2] Betts C. Benefits of metal foams and developments in modelling techniques to assess their materials behaviour: a review. Mater Sci Technol 2012;28(2):129–43.
[3] Ashby, M.F., et al., *Metal foams: a design guide*. 2000: Elsevier.
[4] Gibson LJ. Mechanical behavior of metallic foams. Annu Rev Mater Sci 2000;30(1): 191–227.
[5] Ji S, Gu Qi, Xia B. Porosity dependence of mechanical properties of solid materials. J Mater Sci 2006;41(6):1757–68.
[6] Magnucki K, Malinowski M, Kasprzak J. Bending and buckling of a rectangular porous plate. Steel Compos Struct 2006;6(4):319–33.
[7] Chen D, Yang J, Kitipornchai S. Elastic buckling and static bending of shear deformable functionally graded porous beam. Compos Struct 2015;133:54–61.
[8] Rezaei AS, Saidi AR. Exact solution for free vibration of thick rectangular plates made of porous materials. Compos Struct 2015;134:1051–60.
[9] Arani AG, Khoddami Maraghi Z, Khani M, Alinaghian I. Free vibration of embedded porous plate using third-order shear deformation and poroelasticity theories. J Eng 2017;2017:1–13.
[10] Akbaş ŞD. Vibration and static analysis of functionally graded porous plates. J Appl Comput Mech 2017;3(3):199–207.
[11] Wattanasakulpong N, Chaikittiratana A, Pornpeerakeat S. Chebyshev collocation approach for vibration analysis of functionally graded porous beams based on third-order shear deformation theory. Acta Mech Sin 2018;34(6):1124–35.
[12] Phuong NTB, Tu TM, Phuong HT, Long NV. Bending analysis of functionally graded beam with porosities resting on elastic foundation based on neutral surface position. J Sci Technol Civ Eng (STCE)-NUCE 2019;13(1):33–45.
[13] Demirhan PA, Taskin V. Bending and free vibration analysis of Levy-type porous functionally graded plate using state space approach. Compos B Eng 2019;160: 661–76.
[14] Zhao J, Wang Q, Deng X, Choe K, Zhong R, Shuai C. Free vibrations of functionally graded porous rectangular plate with uniform elastic boundary conditions. Compos B Eng 2019;168:106–20.
[15] Rad ES, et al. Shear deformation theories for elastic buckling of fluid-infiltrated porous plates: An analytical approach. Compos Struct 2020;254:112829.
[16] Shen H-S. Nonlinear bending response of functionally graded plates subjected to transverse loads and in thermal environments. Int J Mech Sci 2002;44(3):561–84.
[17] Na K-S, Kim J-H. Nonlinear bending response of functionally graded plates under thermal loads. J Therm Stresses 2006;29(3):245–61.
[18] Yu TT, Yin S, Bui TQ, Hirose S. A simple FSDT-based isogeometric analysis for geometrically nonlinear analysis of functionally graded plates. Finite Elem Anal Des 2015;96:1–10.
[19] Dong YH, Li YH. A unified nonlinear analytical solution of bending, buckling and vibration for the temperature-dependent FG rectangular plates subjected to thermal load. Compos Struct 2017;159:689–701.
[20] Kumar A, Singha MK, Tiwari V. Nonlinear bending and vibration analyses of quadrilateral composite plates. Thin-Walled Structures 2017;113:170–80.
[21] Gholami R, Ansari R. Large deflection geometrically nonlinear analysis of functionally graded multilayer graphene platelet-reinforced polymer composite rectangular plates. Compos Struct 2017;180:760–71.
[22] Nguyen NV, Nguyen HX, Lee S, Nguyen-Xuan H. Geometrically nonlinear polygonal finite element analysis of functionally graded porous plates. Adv Eng Softw 2018;126:110–26.
[23] Dinh Duc N, et al. Nonlinear dynamic response of functionally graded porous plates on elastic foundation subjected to thermal and mechanical loads. J Appl Comput Mech 2018;4(4):245–59.
[24] Cong PH, Chien TM, Khoa ND, Duc ND. Nonlinear thermomechanical buckling and post-buckling response of porous FGM plates using Reddy's HSDT. Aerosp Sci Technol 2018;77:419–28.
[25] Huang X-L, et al. Nonlinear free and forced vibrations of porous sigmoid functionally graded plates on nonlinear elastic foundations. Compos Struct 2019; 228:111326.
[26] Li K, Wu Di, Chen X, Cheng J, Liu Z, Gao W, et al. Isogeometric analysis of functionally graded porous plates reinforced by graphene platelets. Compos Struct 2018;204:114–30.
[27] Keleshteri M, Jelovica J. Nonlinear vibration behavior of functionally graded porous cylindrical panels. Compos Struct 2020;239:112028.
[28] Mirjavadi SS, et al., Geometrically nonlinear vibration analysis of eccentrically stiffened porous functionally graded annular spherical shell segments. Mechanics Based Design of Structures and Machines, 2020: p. 1-15.
[29] Xie K, et al. Large-amplitude nonlinear free vibrations of functionally graded plates with porous imperfection: A novel approach based on energy balance method. Compos Struct 2020;246:112367.
[30] Tu TM, Hoa LK, Hung DX, Hai LT. Nonlinear buckling and post-buckling analysis of imperfect porous plates under mechanical loads. J Sandwich Struct Mater 2020;22 (6):1910–30.
[31] Hung DX, et al. Nonlinear buckling and postbuckling of FG porous variable thickness toroidal shell segments surrounded by elastic foundation subjected to compressive loads. Aerosp Sci Technol 2020;107:106253.
[32] Ansari R, et al. Nonlinear bending analysis of arbitrary-shaped porous nanocomposite plates using a novel numerical approach. Int J Non Linear Mech 2020;126:103556.
[33] Liu T, et al. Geometrically nonlinear isogeometric analysis of smart piezoelectric FG plates considering thermal effects of piezoelectric stress and dielectric constants. Compos Struct 2021;266:113795.
[34] Mahesh V, Harursampath D. Large deflection analysis of functionally graded magneto-electro-elastic porous flat panels. Eng Comput 2021:1–20.
[35] Chen Da, Yang J, Kitipornchai S. Free and forced vibrations of shear deformable functionally graded porous beams. Int J Mech Sci 2016;108-109:14–22.
[36] Barati MR, Zenkour AM. Investigating post-buckling of geometrically imperfect metal foam nanobeams with symmetric and asymmetric porosity distributions. Compos Struct 2017;182:91–8.
[37] Zhang D-G. Modeling and analysis of FGM rectangular plates based on physical neutral surface and high order shear deformation theory. Int J Mech Sci 2013;68: 92–104.
[38] Wang CM, Ke LL, Roy Chowdhury AN, Yang J, Kitipornchai S, Fernando D. Critical examination of midplane and neutral plane formulations for vibration analysis of FGM beams. Eng Struct 2017;130:275–81.
[39] Farzam-Rad SA, Hassani B, Karamodin A. Isogeometric analysis of functionally graded plates using a new quasi-3D shear deformation theory based on physical neutral surface. Compos B Eng 2017;108:174–89.
[40] Reddy JN. *Theory and analysis of elastic plates and shells*. 2006: CRC press.
[41] Reddy JN. *Energy principles and variational methods in applied mechanics*. 2017: John Wiley & Sons.
[42] Brush DO, Almroth BO, Hutchinson J. *Buckling of bars, plates, and shells.* 1975.
[43] Shen H-S. Postbuckling of FGM plates with piezoelectric actuators under thermo-electro-mechanical loadings. Int J Solids Struct 2005;42(23):6101–21.
[44] Kapoor H, Kapania RK. Geometrically nonlinear NURBS isogeometric finite element analysis of laminated composite plates. Compos Struct 2012;94(12): 3434–47.
[45] Lei X-Y, Huang M-K, Wang X. Geometrically nonlinear analysis of a Reissner type plate by the boundary element method. Comput Struct 1990;37(6):911–6.
[46] Azizian ZG, Dawe DJ. Geometrically nonlinear analysis of rectangular mindlin plates using the finite strip method. Comput Struct 1985;21(3):423–36.